Impact of rift history on the structural style of intracontinental rift-inversion orogens

Dylan A. Vasey[1,2], John B. Naliboff[3], Eric Cowgill[1], Sascha Brune[4,5], Anne Glerum[4], and Frank Zwaan[4,6]

[1]Department of Earth and Planetary Sciences, University of California, Davis, CA 95616

[2]Department of Earth and Climate Sciences, Tufts University, Medford, MA 02155

[3]Department of Earth and Environmental Science, New Mexico Institute of Mining and Technology, Socorro, NM 87801

[4]GFZ German Research Centre for Geosciences, Telegrafenberg, 14473 Potsdam, Germany

[5]Institute of Geosciences, University of Potsdam, 14476 Potsdam-Golm, Germany

[6]Department of Geosciences, University of Fribourg, 1700 Fribourg, Switzerland

This manuscript has been submitted for publication in GEOLOGY. This version has been revised once in response to peer review and has been resubmitted. It is currently under review and has yet to be formally accepted for publication. Subsequent versions of this manuscript may have slightly different content. If accepted, the final version of this manuscript will be available via the "Peer-reviewed Publication DOI" link on the right-hand side of this webpage. Please feel free to contact any of the authors; we welcome feedback.

Corresponding Author: Dylan Vasey (Dylan.Vasey@tufts.edu)

Impact of rift history on the structural style of intracontinental rift-inversion orogens

Dylan A. Vasey[1,2], John B. Naliboff[3], Eric Cowgill[1], Sascha Brune[4,5], Anne Glerum[4], and Frank Zwaan[4,6]

[1]Department of Earth and Planetary Sciences, University of California, Davis, CA 95616

[2]Department of Earth and Climate Sciences, Tufts University, Medford, MA 02155

[3]Department of Earth and Environmental Science, New Mexico Institute of Mining and Technology, Socorro, NM 87801

[4]GFZ German Research Centre for Geosciences, Telegrafenberg, 14473 Potsdam, Germany

[5]Institute of Geosciences, University of Potsdam, 14476 Potsdam-Golm, Germany

[6]Department of Geosciences, University of Fribourg, 1700 Fribourg, Switzerland

ABSTRACT

Although many collisional orogens form after subduction of oceanic lithosphere between two continents, some orogens result from strain localization within a continent via inversion of structures inherited from continental rifting. Intracontinental rift-inversion orogens exhibit a range of structural styles, but the underlying causes of such variability have not been extensively explored. Here, we use numerical models of intracontinental rift inversion to investigate the impact of parameters including rift structure, rift duration, post-rift cooling, and convergence velocity on orogen structure. Our models reproduce the natural variability of rift-inversion orogens and can be categorized using three endmember styles: asymmetric underthrusting (AU), distributed thickening (DT), and localized polarity flip (PF). Inversion of narrow rifts tends to produce orogens with more localized deformation (Styles AU and PF) than those resulting from

wide rifts. However, multiple combinations of the parameters we investigated can produce the same structural style. Thus, our models indicate no unique relationship between orogenic structure and the conditions prior to and during inversion. Because the style of rift-inversion orogenesis is highly contingent upon the rift history prior to inversion, knowing the geologic history that preceded rift inversion is essential for translating orogenic structure into the processes that produced that structure.

INTRODUCTION

Plate-boundary collisional orogens form along boundaries between tectonic plates when two continental blocks collide following subduction of intervening oceanic lithosphere (e.g., Dewey and Bird, 1970). In contrast, intraplate orogens form within a continental plate by localization of strain along pre-existing weaknesses (e.g., Vilotte et al., 1982; Ziegler et al., 1995; Raimondo et al., 2014). Some intraplate orogens reactivate weaknesses inherited from past collisions (e.g., Tien Shan; Jourdon et al., 2018), whereas others exploit weaknesses developed during continental rifting and thus are considered the result of rift inversion (Fig 1; e.g., Cooper et al., 1989; Beauchamp et al., 1996; Marshak et al., 2000). A common presumption seems to be that the structural style of intracontinental rift-inversion orogens should be distinct from that of plate-boundary orogens, because during rift inversion, convergence is expected to occur by reactivation of extensional structures, resulting in distributed lithospheric thickening (e.g., Buiter et al., 2009; Vincent et al., 2016, 2018). However, many rift-inversion orogens feature asymmetric underthrusting along lithosphere-scale shear zones and development of major fold-thrust systems (Fig. 1; e.g., Jammes et al., 2009), comparable to plate-boundary orogens (e.g., Willett et al., 1993; Beaumont et al., 1996).

Geodynamic numerical modeling of rift-inversion orogenesis typically focuses on the High Atlas and Pyrenees (e.g., Buiter et al., 2009; Jammes et al., 2014; Dielforder et al., 2019; Jourdon et al., 2019; Wolf et al., 2021), though the structural styles of these orogens are distinct (Fig. 1). The High Atlas is broadly symmetric, flanked on both sides by fold-thrust belts of opposing vergence, and exhibits no underthrusting of one block of lithosphere beneath another (e.g., Beauchamp et al., 1999; Gomez et al., 2000). In contrast, the Pyrenees show asymmetric lithospheric underthrusting and fold-thrust belt development concentrated on one side of the orogen (e.g., Muñoz, 1992; Dielforder et al., 2019). The structure of these orogens varies considerably along-strike, and other rift-inversion orogens exhibit a range of symmetry and thrust-belt vergence (Fig. 1; e.g., Greater Caucasus, Alice Springs, Araçuai-West Congo, Rocas Verdes; Philip et al., 1989; Fosdick et al., 2011; Raimondo et al., 2014; Fossen et al., 2020), but the controls on this variability are poorly understood.

Here, we present 2D geodynamic numerical models designed to explore connections between the initial conditions of a rift prior to inversion and the structure of the resulting rift-inversion orogen. We find that changes in rift structure, rift duration, post-rift cooling, and convergence velocity dramatically change the large-scale structure of the resulting orogen, producing models that exhibit the distributed lithospheric thickening of the High Atlas, the asymmetric lithospheric underthrusting of the Pyrenees, and additional variability reminiscent of other natural rift-inversion orogens.

GEODYNAMIC MODELING OF RIFT-INVERSION OROGENESIS

We modeled 2D intracontinental rift inversion using the open-source, finite-element code ASPECT (Kronbichler et al., 2012; Heister et al., 2017; Naliboff et al., 2020; Bangerth et al., 2021; see the Supplemental Material for detailed methods[1]). To systematically compare the

competing effects of rift structure, rift duration, post-rift cooling, and convergence rate, we performed 16 model simulations in a 1000 x 600 km model domain (Fig. 2a, Table 1). Each model began by using different combinations of lithospheric thickness and extension velocity to develop either a narrow or wide rift structure from an initial block of continental lithosphere (Fig. 2b, Table 1; e.g., Tetreault and Buiter, 2018). We stopped extension either at lithospheric breakup or at half the model time required to reach breakup. We inverted each of these four rifts with either no post-rift cooling phase or after a cooling period of 20 Myr to get an initial sense of the effects of a post-rift cooling phase on orogenic style. For each of these eight models, we imposed two different convergence velocities during inversion (1 cm/yr, 5 cm/yr), with duration scaled (20 Myr, 4 Myr) so that each orogen underwent the same amount of total convergence (200 km).

RESULTING STYLES OF RIFT-INVERSION OROGENESIS

Style AU: Asymmetric Underthrusting

Several of our model rift-inversion orogens are characterized by asymmetric underthrusting of one block of lithosphere beneath another along a lithosphere-scale shear zone (Style AU, Fig. 2c). This behavior is exemplified by Model 1, formed from immediate inversion at 1 cm/yr of a narrow rift halfway to lithospheric breakup (Fig. 2a; Table 1). In this model, initial symmetric uplift of both sides of the rift gives way to localization of most strain along a left-dipping shear zone to the right of the former rift axis (Fig. 2c). Near the end of the model run, deformation propagates both along a synthetic shear zone to the right of the main structure and along an antithetic backthrust to the left.

Style DT: Distributed Thickening

By contrast, a second group of models does not localize deformation along lithosphere-scale thrust shear zones but instead undergoes distributed thickening of the lithosphere due to inversion along former normal faults (Style DT). Model 5 (Fig. 2c) demonstrates this deformational style and tracks the immediate inversion at 1 cm/yr of a wide rift that has extended halfway to lithospheric breakup (Fig. 2a, Table 1). Distributed deformation during rifting leaves a ~400-km-wide zone of primarily upper-crustal normal faults with no distinct rift axis. Compression during inversion leads to reactivation of these structures as reverse faults as the lower crust and mantle lithosphere buckle and fold.

Style PF: Localized Polarity Flip

In a third set of models, deformation is localized asymmetrically along lithosphere-scale shear zones, but the individual shear zones are short-lived and are crosscut as new shear zones of opposite polarity take over (Style PF). An endmember case of this orogenic style is Model 3 (Fig. 2c), which results from immediate inversion at 1 cm/yr of a narrow rift at full lithospheric breakup (Fig. 2a; Table 1). In this case, initial symmetric asthenospheric upwelling at the rift axis gives way to localized deformation along two right-dipping, lithosphere-scale shear zones that are then subsequently crosscut by left-dipping shear zones. The resulting orogen is largely symmetric with only a hint of right-directed vergence (Fig. 2c).

Intermediate Modes of Orogenic Style

Half of the model results can be classified as distinctly Style AU, DT, or PF rift-inversion orogens, while the other half exhibit orogenesis that is intermediate in character (Fig. 3). Intermediate behavior generally results from increasing localization of deformation as inversion proceeds, with Style DT leading to Style PF (Model 15) or Style AU (Models 6, 7, 8, and 14) and Style PF leading to Style AU (Models 2 and 10). The exception to this trend is Model 4, in

which initial localization along a pair of left- and right-dipping shear zones (Style PF) gives way to more distributed deformation (Style DT).

CORRELATIONS BETWEEN INITIAL CONDITIONS AND STRUCTURAL STYLE

To visualize the relationship between the model parameters explored here and the resulting structural styles, we assign each model a place on a schematic ternary diagram with vertices representing Styles AU, DT, and PF (Fig. 3). We additionally place each of the natural orogens presented in Fig. 1 on this diagram based on the overall vergence of major structures in the final orogen. The configuration of each individual orogen is contingent on the specific ensemble of parameters that produced it. However, there are general patterns between individual parameters and our three endmember orogenic styles.

The greatest influence on orogenic style is exerted by the structure of the rift (Fig. 3). Rift-inversion orogens that start with a narrow rift tend to have more localized deformation along lithosphere-scale shear zones, resulting in pronounced asymmetric underthrusting (Style AU) or flipping polarity (Style PF). By contrast, inversion of a wide rift tends to result in orogens with more distributed thickening (Style DT). However, this pattern does not hold across the full range of parameter space, with one orogen formed from a narrow rift (Model 4) exhibiting elements of distributed thickening (Style DT) and several orogens formed from wide rifts (Models 6, 7, 8, 14, 15, 16) displaying at least some element of Styles AU or PF.

The influence of post-rift cooling and rift duration is less systematic. Rifting to full lithospheric breakup rather than halfway to breakup promotes localized deformation (Styles AU and PF), though this is highly contingent on the rift structure (Fig. 3). Full breakup in a narrow rift tends to promote Style PF over Style AU (e.g., Models 3, 12), whereas inversion of a wide rift after full breakup promotes Style AU over Style DT (e.g., Models 7, 8, 16). Post-rift cooling

promotes increasing localization of deformation (Styles AU and PF). For inversion of narrow rifts (e.g., Models 2, 10, 12), the post-rift cooling phase tends to result in shear zones of alternating polarity (Style PF) rather than asymmetric underthrusting (Style AU), whereas for inversion of wide rifts (e.g., Models 6, 14, 16), post-rift cooling tends to result in more distinctly asymmetric (Style AU) behavior (Fig. 3).

The convergence velocity has less of an impact on the structure of the resulting orogen, but in general, faster convergence velocities appear to promote asymmetric underthrusting (Style AU). The most striking influence is seen by comparing Models 3 (1 cm/yr) and 11 (5 cm/yr), which are equivalent in setup apart from convergence velocity. Model 3 is our exemplar orogen for Style PF (Fig. 2c), whereas Model 11 exhibits asymmetric underthrusting representative of Style AU (Fig. 3).

COMPARISONS WITH PRIOR MODELING AND NATURAL EXAMPLES

Our study differs from prior work by exploring the range of structural variability in rift inversion orogenesis as a general process (see Supplementary Material for additional details[1]). Studies focused on the Pyrenees tend to feature narrow rift structures taken close to lithospheric breakup with no post-rift cooling, resulting in orogens that resemble Style AU (Jammes et al., 2014; Dielforder et al., 2019; Jourdon et al., 2019). Some modeling studies of continental collision include one or more rift-inversion orogens for comparison with models with no pre-collisional extension, using parameters similar to the Pyrenees models that also yield Style AU orogens (Jammes and Huismans, 2012; Wolf et al., 2021). One study that emphasizes the High Atlas includes wide rifts extended part way to lithospheric breakup with significant post-rift cooling, with resulting orogens exhibiting Style DT (Buiter et al., 2009). By exploring a wider range of first-order variations in initial rift conditions, we capture both the AU orogenic style

seen in models of the Pyrenees and the DT style seen in the Atlas-inspired model within a single suite of model results, in addition to other modes of deformation (Style PF and intermediate modes) that do not resemble the High Atlas or Pyrenees (Fig. 3).

This initial exploration suggests that the path to developing a particular structural style is non-unique; different combinations of rift structure, rift duration, post-rift cooling, and/or convergence velocity can result in the same first-order style (Fig. 3). Thus, in natural intracontinental rift-inversion orogens, the observed structural style may provide some indication of initial conditions but cannot uniquely pinpoint a single set of conditions. For example, the asymmetric underthrusting (Style AU) observed in the Pyrenees or western Greater Caucasus (Fig. 1) could potentially be produced both by slower closure of a narrow rift immediately after partial lithospheric breakup (Model 1) or by faster closure of a narrow rift extended to full lithospheric breakup (Model 11).

Since the present-day structure of these orogens alone is insufficient to uniquely identify these parameters, using additional observations to constrain their geologic histories is critical. This study highlights the need to collect data that can differentiate between incremental tectonic histories in natural orogens. In particular, we note the importance of low-temperature thermochronology, which can provide constraints on both the timing and magnitude of deformation across major structures within collisional orogens (e.g., McQuarrie and Ehlers, 2017), as well as sedimentary records, which track changes in deposition and erosion as rifting and collision proceed (e.g., Tye et al., 2020). Future modeling studies that connect these first-order structural styles and their rift histories with patterns in thermochronology and/or sedimentary basin evolution will be essential for unraveling the complete history of intracontinental rift-inversion orogens.

CONCLUSIONS

2D geodynamic numerical modeling of intracontinental rift inversion indicates that the structural style of rift-inversion orogens is highly dependent on initial conditions, including rift structure, rift duration, post-rift cooling, and convergence velocity. Model orogens resulting from variations in these parameters can be classified using three structural styles: asymmetric underthrusting (AU), distributed thickening (DT), and localized polarity flip (PF). No systematic relationship exists between structural style and individual parameters, though narrow rifts, rifts that do not achieve lithospheric breakup, and rifts that cool prior to inversion tend to promote localized deformation (AU and PF) over distributed deformation (DT). These model results reconcile the range of structural styles seen in natural rift-inversion orogens but also indicate that a single structural style can be produced from multiple rift histories.

ACKNOWLEDGMENTS

This study was supported by NSF grant 2050623 to Cowgill. ASPECT is hosted by CIG, supported by NSF grants 0949446 and 1550901. This work primarily used XSEDE (Towns et al., 2014) allocations EES210024 (Cowgill) and EAR080022N (CIG) on Stampede2, supported by NSF grant 1548562. Additional models were run using ACCESS (Boerner et al., 2023) allocations EES230094 (Vasey) and TRA130003 (Tufts) on the Expanse, supported by NSF grants 2138259, 2138286, 2138307, 2137603, and 2138296. We thank L. Le Pourhiet and two anonymous reviewers for constructive reviews.

REFERENCES CITED

Bangerth, W., Dannberg, J., Fraters, M., Gassmoeller, R., Glerum, A., Heister, T., and Naliboff, J., 2021, ASPECT v2.3.0:, https://doi.org/10.5281/ZENODO.5131909.

Beauchamp, W., Allmendinger, R.W., Barazangi, M., Demnati, A., Alji, M.E., and Dahmani, M., 1999, Inversion tectonics and the evolution of the High Atlas Mountains, Morocco, based

on a geological-geophysical transect: Tectonics, v. 18, p. 163–184, doi:10.1029/1998TC900015.

Beauchamp, W., Barazangi, M., Demnati, A., and Alji, M.E., 1996, Intracontinental Rifting and Inversion: Missour Basin and Atlas Mountains, Morocco: AAPG Bulletin, v. 80, p. 1459–1481, doi:10.1306/64ED9A60-1724-11D7-8645000102C1865D.

Beaumont, C., Ellis, S., Hamilton, J., and Fullsack, P., 1996, Mechanical model for subduction-collision tectonics of Alpine-type compressional orogens: Geology, v. 24, p. 675–678, doi:10.1130/0091-7613(1996)024<0675:MMFSCT>2.3.CO;2.

Boerner, T.J., Deems, S., Furlani, T.R., Knuth, S.L., and Towns, J., 2023, ACCESS: Advancing Innovation: NSF's Advanced Cyberinfrastructure Coordination Ecosystem: Services & Support, *in* Practice and Experience in Advanced Research Computing, New York, NY, USA, Association for Computing Machinery, PEARC '23, p. 173–176, doi:10.1145/3569951.3597559.

Buiter, S.J.H., Pfiffner, O.A., and Beaumont, C., 2009, Inversion of extensional sedimentary basins: A numerical evaluation of the localisation of shortening: Earth and Planetary Science Letters, v. 288, p. 492–504, doi:10.1016/j.epsl.2009.10.011.

Cooper, M.A., Williams, G.D., Graciansky, P.C. de, Murphy, R.W., Needham, T., Paor, D. de, Stoneley, R., Todd, S.P., Turner, J.P., and Ziegler, P.A., 1989, Inversion tectonics - A discussion: Geological Society, London, Special Publications, v. 44, p. 335–347, doi:10.1144/GSL.SP.1989.044.01.18.

Dewey, J.F., and Bird, J.M., 1970, Mountain belts and the new global tectonics: Journal of Geophysical Research, v. 75, p. 2625–2647, doi:10.1029/JB075i014p02625.

Dielforder, A., Frasca, G., Brune, S., and Ford, M., 2019, Formation of the Iberian-European convergent plate boundary fault and its effect on intraplate deformation in Central Europe: Geochemistry, Geophysics, Geosystems, v. 20, p. 2395–2417, doi:10.1029/2018GC007840.

Fosdick, J.C., Romans, B.W., Fildani, A., Bernhardt, A., Calderón, M., and Graham, S.A., 2011, Kinematic evolution of the Patagonian retroarc fold-and-thrust belt and Magallanes foreland basin, Chile and Argentina, 51°30′S: GSA Bulletin, v. 123, p. 1679–1698, doi:10.1130/B30242.1.

Fossen, H., Cavalcante, C., Konopásek, J., Meira, V.T., de Almeida, R.P., Hollanda, M.H.B.M., and Trompette, R., 2020, A critical discussion of the subduction-collision model for the Neoproterozoic Araçuaí-West Congo orogen: Precambrian Research, v. 343, p. 105715, doi:10.1016/j.precamres.2020.105715.

Gomez, F., Beauchamp, W., and Barazangi, M., 2000, Role of the Atlas Mountains (northwest Africa) within the African-Eurasian plate-boundary zone: Geology, v. 28, p. 775–778, doi:10.1130/0091-7613(2000)28<775:ROTAMN>2.0.CO;2.

Heister, T., Dannberg, J., Gassmöller, R., and Bangerth, W., 2017, High accuracy mantle convection simulation through modern numerical methods – II: realistic models and problems: Geophysical Journal International, v. 210, p. 833–851, doi:10.1093/gji/ggx195.

Jammes, S., and Huismans, R.S., 2012, Structural styles of mountain building: Controls of lithospheric rheologic stratification and extensional inheritance: Journal of Geophysical Research: Solid Earth, v. 117, doi:10.1029/2012JB009376.

Jammes, S., Huismans, R.S., and Muñoz, J.A., 2014, Lateral variation in structural style of mountain building: controls of rheological and rift inheritance: Terra Nova, v. 26, p. 201–207, doi:10.1111/ter.12087.

Jammes, S., Manatschal, G., Lavier, L., and Masini, E., 2009, Tectonosedimentary evolution related to extreme crustal thinning ahead of a propagating ocean: Example of the western Pyrenees: Tectonics, v. 28, doi:https://doi.org/10.1029/2008TC002406.

Jourdon, A., Le Pourhiet, L., Mouthereau, F., and Masini, E., 2019, Role of rift maturity on the architecture and shortening distribution in mountain belts: Earth and Planetary Science Letters, v. 512, p. 89–99, doi:10.1016/j.epsl.2019.01.057.

Jourdon, A., Le Pourhiet, L., Petit, C., and Rolland, Y., 2018, The deep structure and reactivation of the Kyrgyz Tien Shan: Modelling the past to better constrain the present: Tectonophysics, v. 746, p. 530–548, doi:10.1016/j.tecto.2017.07.019.

Kronbichler, M., Heister, T., and Bangerth, W., 2012, High accuracy mantle convection simulation through modern numerical methods: Geophysical Journal International, v. 191, p. 12–29, doi:10.1111/j.1365-246X.2012.05609.x.

Marshak, S., Karlstrom, K., and Timmons, J.M., 2000, Inversion of Proterozoic extensional faults: An explanation for the pattern of Laramide and Ancestral Rockies intracratonic deformation, United States: Geology, v. 28, p. 735–738, doi:10.1130/0091-7613(2000)28<735:IOPEFA>2.0.CO;2.

McQuarrie, N., and Ehlers, T.A., 2017, Techniques for understanding fold-and-thrust belt kinematics and thermal evolution, *in* Law, R.D., Thigpen, J.R., Merschat, A.J., and Stowell, H. eds., Linkages and Feedbacks in Orogenic Systems, Geological Society of America Memoir 213, p. 1–30.

Muñoz, J.A., 1992, Evolution of a continental collision belt: ECORS-Pyrenees crustal balanced cross-section, *in* McClay, K.R. ed., Thrust Tectonics, Dordrecht, Springer Netherlands, p. 235–246, doi:10.1007/978-94-011-3066-0_21.

Naliboff, J.B., Glerum, A., Brune, S., Péron-Pinvidic, G., and Wrona, T., 2020, Development of 3-D Rift Heterogeneity Through Fault Network Evolution: Geophysical Research Letters, v. 47, p. e2019GL086611, doi:https://doi.org/10.1029/2019GL086611.

Philip, H., Cisternas, A., Gvishiani, A., and Gorshkov, A., 1989, The Caucasus: An actual example of the initial stages of continental collision: Tectonophysics, v. 161, p. 1–21, doi:10.1016/0040-1951(89)90297-7.

Raimondo, T., Hand, M., and Collins, W.J., 2014, Compressional intracontinental orogens: Ancient and modern perspectives: Earth-Science Reviews, v. 130, p. 128–153, doi:10.1016/j.earscirev.2013.11.009.

Tetreault, J.L., and Buiter, S.J.H., 2018, The influence of extension rate and crustal rheology on the evolution of passive margins from rifting to break-up: Tectonophysics, v. 746, p. 155–172, doi:10.1016/j.tecto.2017.08.029.

Towns, J. et al., 2014, XSEDE: Accelerating Scientific Discovery: Computing in Science & Engineering, v. 16, p. 62–74, doi:10.1109/MCSE.2014.80.

Tye, A.R., Niemi, N.A., Safarov, R.T., Kadirov, F.A., and Babayev, G.R., 2020, Sedimentary response to a collision orogeny recorded in detrital zircon provenance of Greater Caucasus foreland basin sediments: Basin Research, doi:10.1111/bre.12499.

Vilotte, J.P., Daignières, M., and Madariaga, R., 1982, Numerical modeling of intraplate deformation: Simple mechanical models of continental collision: Journal of Geophysical Research: Solid Earth, v. 87, p. 10709–10728, doi:https://doi.org/10.1029/JB087iB13p10709.

Vincent, S.J., Braham, W., Lavrishchev, V.A., Maynard, J.R., and Harland, M., 2016, The formation and inversion of the western Greater Caucasus Basin and the uplift of the western Greater Caucasus: Implications for the wider Black Sea region: Tectonics, v. 35, p. 2948–2962, doi:10.1002/2016TC004204.

Vincent, S.J., Saintot, A., Mosar, J., Okay, A.I., and Nikishin, A.M., 2018, Comment on “Relict basin closure and crustal shortening budgets during continental collision: An example from Caucasus sediment provenance” by Cowgill et al. (2016): Tectonics, v. 37, p. 1006–1016, doi:10.1002/2017TC004515.

Willett, S., Beaumont, C., and Fullsack, P., 1993, Mechanical model for the tectonics of doubly vergent compressional orogens: Geology, v. 21, p. 371–374, doi:10.1130/0091-7613(1993)021<0371:MMFTTO>2.3.CO;2.

Wolf, S.G., Huismans, R.S., Muñoz, J.-A., Curry, M.E., and Beek, P. van der, 2021, Growth of Collisional Orogens From Small and Cold to Large and Hot—Inferences From Geodynamic Models: Journal of Geophysical Research: Solid Earth, v. 126, p. e2020JB021168, doi:https://doi.org/10.1029/2020JB021168.

Ziegler, P.A., Cloetingh, S., and van Wees, J.-D., 1995, Dynamics of intra-plate compressional deformation: the Alpine foreland and other examples: Tectonophysics, v. 252, p. 7–59, doi:10.1016/0040-1951(95)00102-6.

FIGURE CAPTIONS

Figure 1: Schematic cross-sections of Cenozoic and Pre-Cenozoic rift-inversion orogens ordered by degree of symmetry (adapted from Raimondo et al., 2014; Fossen et al., 2020; Fosdick et al., 2011; Beauchamp et al., 1999; Dielforder et al., 2019; Philip et al., 1989). All orogens shown in present-day configuration, except for Araçuai-West Congo shown at ~600-570 Ma.

Figure 2: a) Graphical overview of parameter space explored by the 16 models in this study. An initial narrow or wide rift is taken either halfway or all the way to lithospheric breakup. The resulting 4 rift structures (color-coded, see Fig. 2b) are inverted immediately (saturated colors) or after 20 Myr of post-rift cooling (faded colors) at either a slower (1 cm/yr; no underline) or faster (5 cm/yr; underlined) convergence rate. **b)** Initial conditions for the model orogens prior to inversion. **c)** Rift inversion results exemplifying structural styles AU, DT, and PF, shown prior to inversion, after 100 km of convergence, and after 200 km of convergence.

Figure 3: Schematic ternary diagram indicating the structural style of each model orogen. Model results shown with the same model area as panels in Fig. 2. Double-headed arrow indicates that rift structure exhibits the strongest control on structural style. Natural examples of rift-inversion orogens are also plotted, showing a similar spread in structural style.

[1]Supplemental Material. Methods, additional tables/figures, and videos of model runs. Please visit https://doi.org/10.1130/XXXX to access the supplemental material, and contact editing@geosociety.org with any questions.

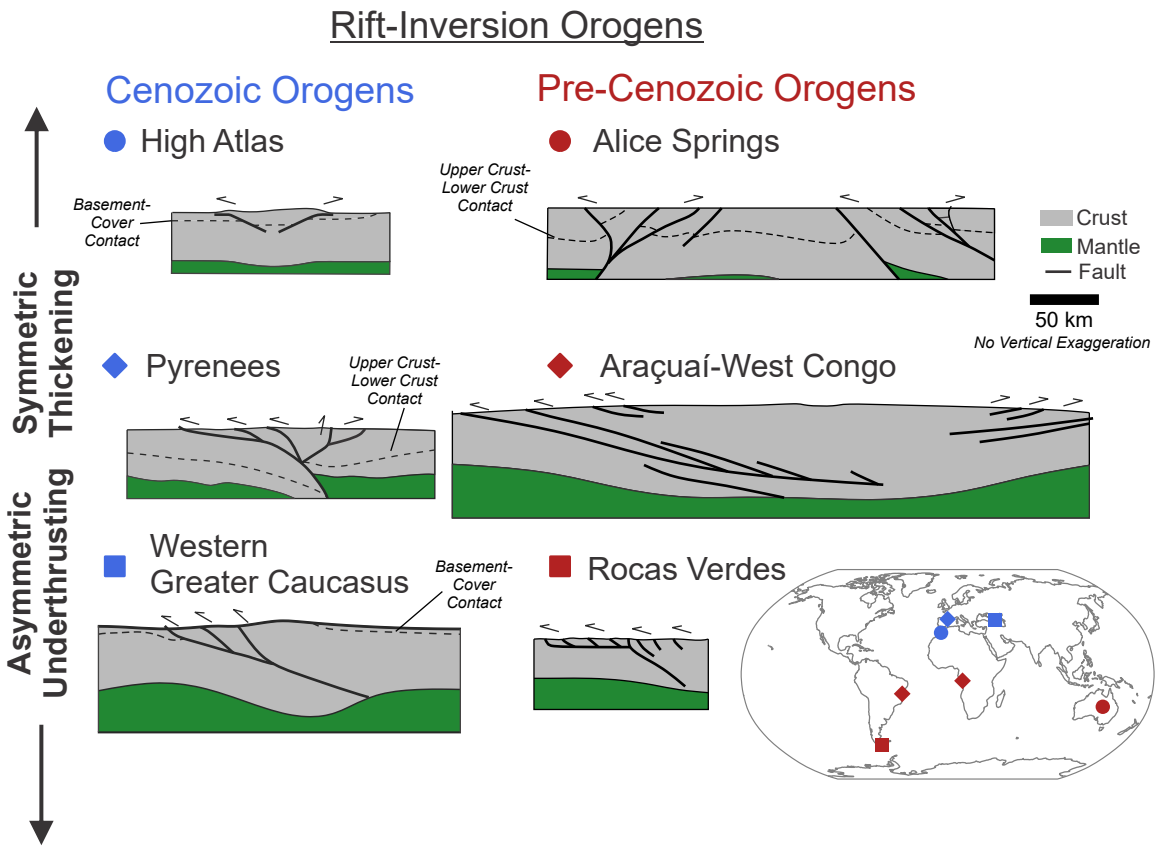
Rift-Inversion Orogens
Cenozoic Orogens
Pre-Cenozoic Orogens
High Atlas
Alice Springs
Basement-Cover Contact
Upper Crust-Lower Crust Contact
Crust
Mantle
Fault
50 km
No Vertical Exaggeration
Symmetric Thickening
Pyrenees
Upper Crust-Lower Crust Contact
Araçuaí-West Congo
Asymmetric Underthrusting
Western Greater Caucasus
Basement-Cover Contact
Rocas Verdes

Figure 1

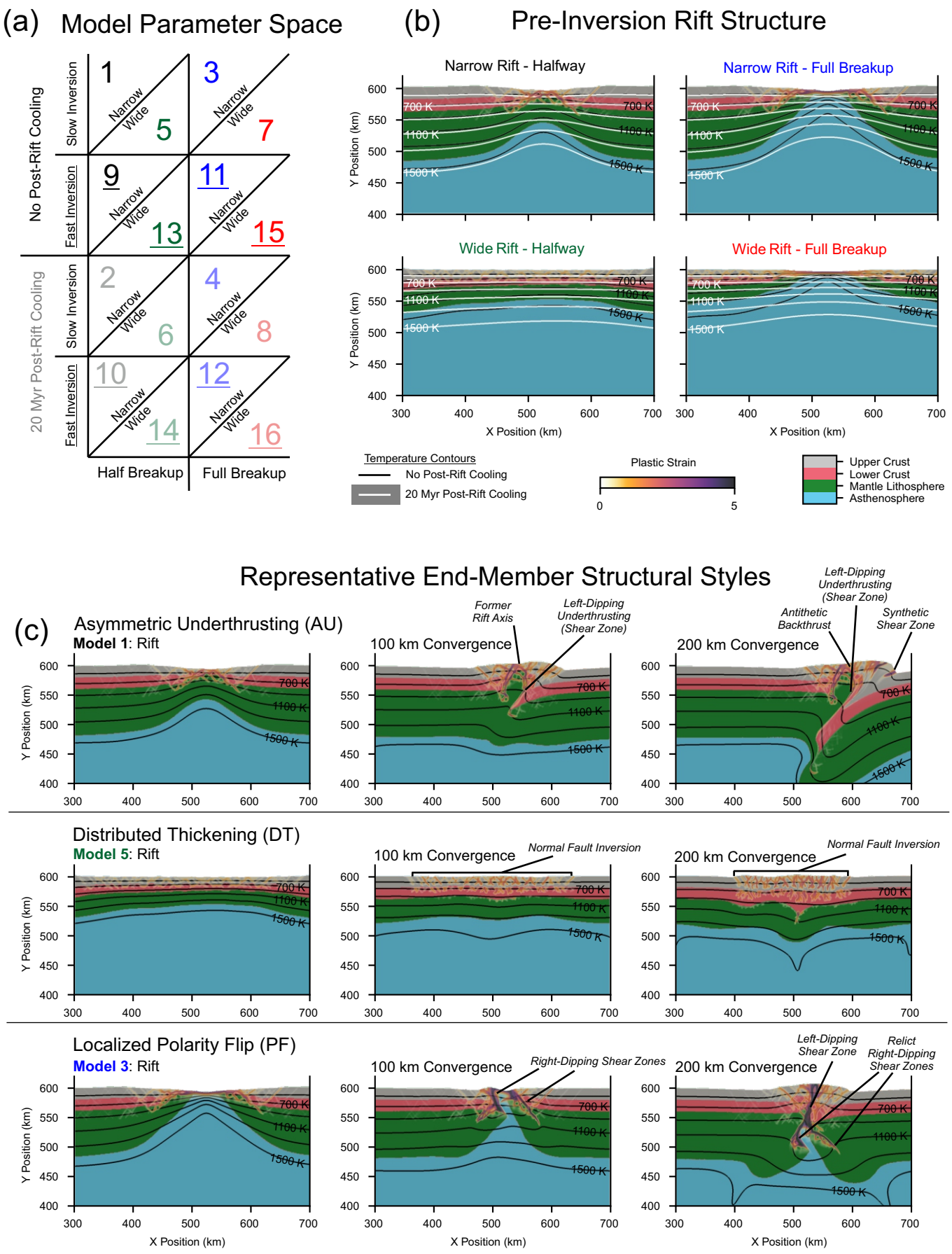
(a) Model Parameter Space
No Post-Rift Cooling
20 Myr Post-Rift Cooling
Slow Inversion
Fast Inversion
Narrow
Wide
Half Breakup
Full Breakup
(b) Pre-Inversion Rift Structure
Narrow Rift - Halfway
Narrow Rift - Full Breakup
Wide Rift - Halfway
Wide Rift - Full Breakup
Y Position (km)
X Position (km)
700 K
1100 K
1500 K
Temperature Contours
No Post-Rift Cooling
20 Myr Post-Rift Cooling
Plastic Strain
Upper Crust
Lower Crust
Mantle Lithosphere
Asthenosphere
Representative End-Member Structural Styles
(c)
Asymmetric Underthrusting (AU)
Model 1: Rift
100 km Convergence
200 km Convergence
Former Rift Axis
Left-Dipping Underthrusting (Shear Zone)
Antithetic Backthrust
Synthetic Shear Zone
Distributed Thickening (DT)
Model 5: Rift
Normal Fault Inversion
Localized Polarity Flip (PF)
Model 3: Rift
Right-Dipping Shear Zones
Left-Dipping Shear Zone
Relict Right-Dipping Shear Zones

Figure 2

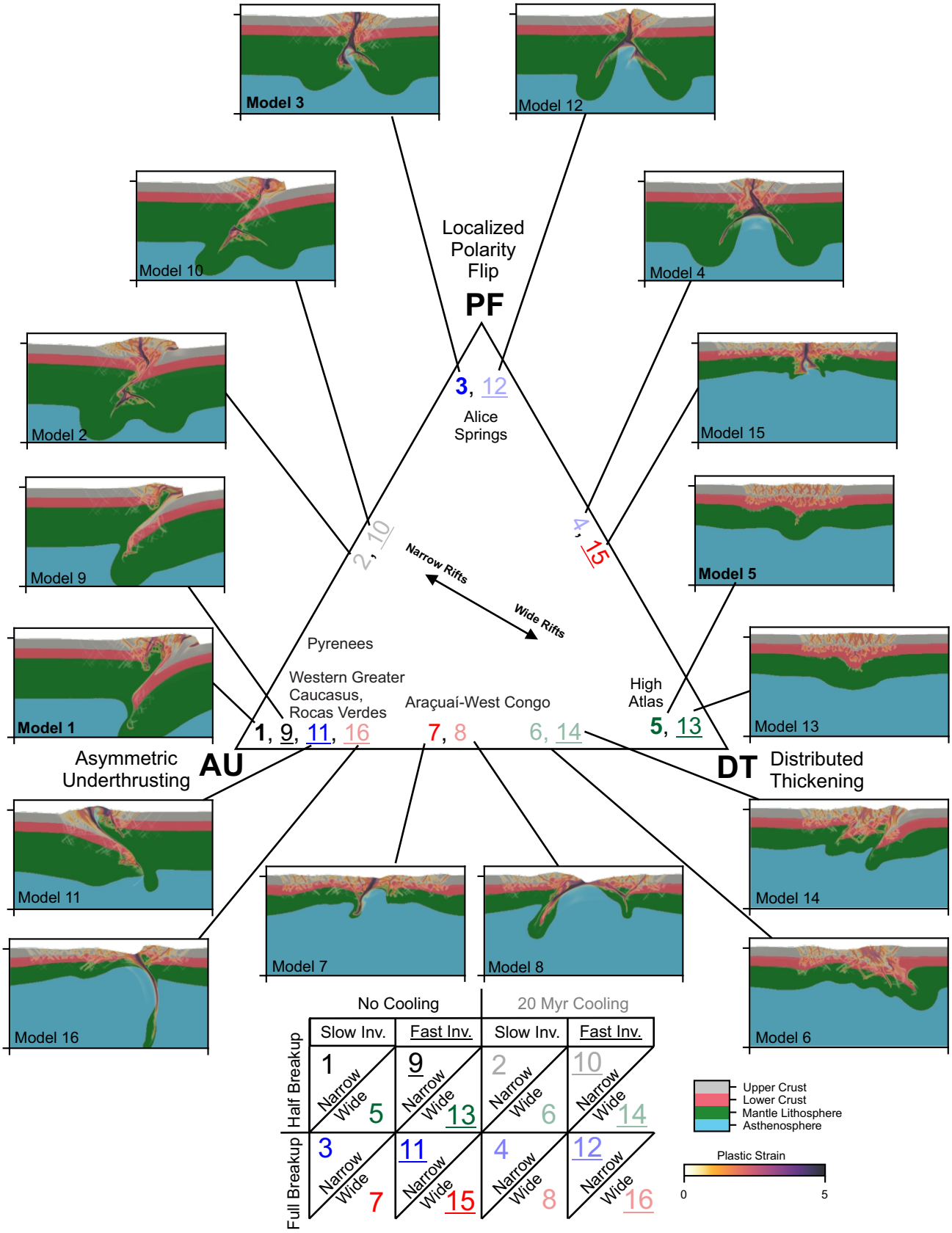
Model 3
Model 12
Model 10
Model 4
Localized
Polarity
Flip
PF
3, 12
Alice
Springs
Model 2
Model 15
Model 9
Model 5
2, 10
4, 15
Narrow Rifts
Wide Rifts
Pyrenees
Western Greater
Caucasus,
Rocas Verdes
Araçuaí-West Congo
High
Atlas
Model 1
1, 9, 11, 16
7, 8
6, 14
5, 13
Model 13
Asymmetric
Underthrusting
AU
DT
Distributed
Thickening
Model 11
Model 14
Model 7
Model 8
Model 16
Model 6
No Cooling
20 Myr Cooling
Slow Inv.
Fast Inv.
Slow Inv.
Fast Inv.
Half Breakup
Full Breakup
1
Narrow
Wide
5
9
Narrow
Wide
13
2
Narrow
Wide
6
10
Narrow
Wide
14
3
Narrow
Wide
7
11
Narrow
Wide
15
4
Narrow
Wide
8
12
Narrow
Wide
16
Upper Crust
Lower Crust
Mantle Lithosphere
Asthenosphere
Plastic Strain
0
5

Figure 3

Table 1: Summary of Rift Inversion Model Parameters

Model Number	Model ID	Extension Velocity	Lithosphere Thickness	Rift Duration	Post-Rift Cooling	Inversion Velocity	Inversion Duration	Total Model Duration
1	063022_rip_c	0.5 cm/yr	120 km	Halfway (16 Myr)	0 Myr	1 cm/yr	20 Myr	36 Myr
2	071822_rip_b	0.5 cm/yr	120 km	Halfway (16 Myr)	20 Myr	1 cm/yr	20 Myr	56 Myr
3	070422_rip_e	0.5 cm/yr	120 km	Full Breakup (32 Myr)	0 Myr	1 cm/yr	20 Myr	52 Myr
4	072022_rip_a	0.5 cm/yr	120 km	Full Breakup (32 Myr)	20 Myr	1 cm/yr	20 Myr	72 Myr
5	070422_rip_c	2 cm/yr	80 km	Halfway (7.3 Myr)	0 Myr	1 cm/yr	20 Myr	27.3 Myr
6	071322_rip	2 cm/yr	80 km	Halfway (7.3 Myr)	20 Myr	1 cm/yr	20 Myr	47.3 Myr
7	070622_rip_a	2 cm/yr	80 km	Full Breakup (14.5 Myr)	0 Myr	1 cm/yr	20 Myr	34.5 Myr
8	072022_rip_b	2 cm/yr	80 km	Full Breakup (14.5 Myr)	20 Myr	1 cm/yr	20 Myr	54.5 Myr
9	080122_rip_a	0.5 cm/yr	120 km	Halfway (16 Myr)	0 Myr	5 cm/yr	3.4 Myr*	19.4 Myr
10	080122_rip_e	0.5 cm/yr	120 km	Halfway (16 Myr)	20 Myr	5 cm/yr	3.5 Myr*	39.5 Myr
11	080122_rip_b	0.5 cm/yr	120 km	Full Breakup (32 Myr)	0 Myr	5 cm/yr	4 Myr	36 Myr
12	080122_rip_f	0.5 cm/yr	120 km	Full Breakup (32 Myr)	20 Myr	5 cm/yr	4 Myr	56 Myr
13	080122_rip_c	2 cm/yr	80 km	Halfway (7.3 Myr)	0 Myr	5 cm/yr	4 Myr	11.3 Myr
14	080122_rip_g	2 cm/yr	80 km	Halfway (7.3 Myr)	20 Myr	5 cm/yr	4 Myr	31.3 Myr
15	080122_rip_d	2 cm/yr	80 km	Full Breakup (14.5 Myr)	0 Myr	5 cm/yr	4 Myr	18.5 Myr
16	080122_rip_h	2 cm/yr	80 km	Full Breakup (14.5 Myr)	20 Myr	5 cm/yr	4 Myr	38.5 Myr

*Models 9 and 10 failed to numerically converge prior to completion of the inversion stage and did not experience the full 200 km of inversion.

Impact of initial conditions on the structural style of intracontinental rift-inversion orogens

Dylan A. Vasey, John B. Naliboff, Eric Cowgill, Sascha Brune, Anne Glerum, Frank Zwaan

Supplemental Material

Contents of This Document:

Text S1
Tables S1 and S2
Figures S1-S4

Separate File:

Compressed folder (.zip) containing videos of each model rift-inversion orogen (Models 1-16) showing compositional field/temperature (same color scheme and contours as in Figs. 2-3), plastic strain, strain rate, and viscosity over time.

Text S1

Numerical Methods

We model 2D continental rift inversion using the open-source, finite-element code ASPECT (Advanced Solver for Problems in Earth's ConvecTion; Kronbichler et al., 2012; Heister et al., 2017; Bangerth et al., 2021), which has been used to model complex processes of lithospheric deformation in a variety of settings (e.g., Glerum et al., 2018, 2020; Fraters and Billen, 2021; Bahadori et al., 2022; Weerdesteijn et al., 2023; Heron et al., 2023; Brune et al., 2023). ASPECT solves equations for the conservation of momentum, mass, and energy, as well as an advection equation for each compositional field. Velocity and pressure are solved for using the extended Boussinesq approximation, with the Stokes equations defined as:

$$\nabla \cdot u = 0 \tag{1}$$

$$-\nabla \cdot \left(2\eta\dot{\epsilon}(u)\right) + \nabla P = \rho g \tag{2}$$

Above, u is velocity, η is viscosity, $\dot{\epsilon}$ is the deviatoric strain rate, P is pressure, ρ is density, and g is gravitational acceleration.

We model temperature evolution with a combination of advection, heat conduction, shear heating, and adiabatic heating:

$$\bar{\rho}C_p\left(\frac{\partial T}{\partial t} + u \cdot \nabla T\right) - \nabla \cdot k\nabla T = \bar{\rho}H + 2\eta\dot{\epsilon}(u) : \dot{\epsilon}(u) + \alpha\bar{\rho}T(u \cdot g) \tag{3}$$

Here, $\bar{\rho}$ is the adiabatic reference density, C_p is heat capacity, T is temperature, t is time, k is thermal conductivity, α is the linear thermal expansion coefficient, and H is the rate of internal

heating. The terms on the right side of the equation correspond to internal heat production, shear heating, and adiabatic heating, respectively.

Density varies linearly as a function of a reference density (ρ_0), a reference temperature (T_0), the linear expansion coefficient, and temperature:

$$\rho = \rho_0\big(1 - \alpha(T - T_0)\big) \tag{4}$$

The rheological behavior combines nonlinear viscous flow with brittle failure (e.g., Glerum et al., 2018):

$$\eta_{eff} = \frac{1}{2} A^{\frac{-1}{n}} d^{\frac{m}{n}} \dot{\epsilon}_e^{\frac{1-n}{n}} e^{\frac{Q+PV}{nRT}} \tag{5}$$

Viscous flow in the crust and mantle lithosphere follows a dislocation creep flow law. In the asthenosphere, viscous flow is a composite of dislocation creep and diffusion creep (Table S1):

$$\eta_{comp} = \frac{\eta_{diff}\eta_{disl}}{\eta_{diff} + \eta_{disl}} \tag{6}$$

Brittle plastic deformation follows a Drucker Prager yield criterion modified to include a plastic damper (e.g., Duretz et al., 2020). This criterion relates the yield stress (σ_y) to the angle of internal friction (ϕ), cohesion (C), viscosity of the plastic damper (η_{vp}), and the viscoplastic strain rate ($\dot{\epsilon}_{vp}$):

$$\sigma_y = C\cos\phi + P\sin\phi + \eta_{vp}\dot{\epsilon}_{vp} \tag{7}$$

Strain softening is implemented by reducing the angle of internal friction and cohesion as a function of accumulated plastic strain. For our models, the initial friction angle is 30° and cohesion is 20 MPa; these values linearly weaken by a factor of 0.375 as a function of finite plastic strain between plastic strain values of 0.5 and 1.5. Following Duretz et al. (2020) and Pan et al. (2022), we use a plastic damper viscosity of 1x 10^{21} Pa s.

The resulting nonlinear set of equations are solved using a solver scheme that includes a single advection step and iterative solves of the Stokes equation through defect Picard iterations to a tolerance of 1 x 10^{-5} (Fraters et al., 2019). The linear system of equations is solved with algebraic multigrid (AMG) scheme, with the linear solver tolerance initially set to 1 x 10^{-7} on the first two iterations and then automatically adjusted to a maximum tolerance of 1 x 10^{-5} (Fraters et al., 2019). Distinct lithologies are tracked using a particle-in-cell scheme (Gassmöller et al., 2018), with each cell initially containing 49 evenly distributed particles and limited to a maximum and minimum and 100 and 24 particles per cell. respectively. Values from the particles are interpolated to the finite element grid using a cell average scheme.

Geodynamic Model Setup

Model Domain and Kinematic Boundary Conditions

The governing equations are solved on a 1000 km by 600 km grid with a resolution of 1 km below the temperature corresponding to a depth of 150 km at the model start, 2 km resolution between 150 and 250 km, and 4 km resolution at temperatures corresponding to depths greater than 250 km at the model start. Such coarsening of the model resolution as a function of temperature ensures the lithosphere and uppermost asthenosphere maintain the same numerical resolution, while also significantly decreasing simulation run times. Significantly, we note that the final stages of the rift inversion and resulting orogen structures are highly sensitive to the adaptive mesh refinement criterion, and we conducted extensive sensitivity tests to ensure our criterion produces the same results as models with constant numerical resolutions, as discussed below.

Deformation is driven by imposing horizontal velocities on the model sides, with inflow/outflow in the top half of the model balanced by equivalent outflow/inflow in the bottom half of the model (Fig. S1). To simulate rift inversion, we first apply a constant extensional velocity to simulate rifting, followed by a period of no velocity to simulate post-rift cooling and then a period of constant convergent velocity to simulate inversion and orogenesis. Varying the magnitude and sign of the boundary velocity terms governs these distinct stages of deformation. The initial extension phase is designed using previous models of long-term continental rifting in ASPECT (e.g., Naliboff et al., 2020; Glerum et al., 2020; Gouiza and Naliboff, 2021; Magni et al., 2021; Brune et al., 2023). The bottom boundary permits free slip and the top boundary is a free surface (Rose et al., 2017), allowing development of topography over time. Erosion and sedimentation on the free surface are approximated using hillslope diffusion with a hillslope transport coefficient of 1×10^{-7} (Sandiford et al., 2021).

Initial Thermal Structure and Thermal Evolution

The initial geothermal structure blends a conductive cooling profile within the lithosphere (Chapman, 1986) with an approximated adiabatic temperature profile that dominates temperature gradients in the convecting mantle. Following previous continental rift models (Naliboff et al., 2017, 2020), we produce a conductive lithospheric temperature profile by prescribing a surface heat flow value that is used to calculate the change in temperature with depth using the thermodynamic properties of each lithospheric layer (Fig. S1). When combined with the approximated adiabatic profile, the surface heat flow can be adjusted to produce a desired lithospheric thickness (e.g., Magni et al., 2021), the base of which is defined by the 1300°C isotherm.

Lithologic Structure and Rheology

The model domain contains distinct compositional layers with unique thermodynamic (reference density, radiogenic heating) and rheologic (flow law) properties (Table S1, Fig. S1). Each layer and additional advected non-lithologic fields (e.g., strain) are tracked using particle-in-cell methods. Following previous models of continental rifting (Naliboff and Buiter, 2015; Naliboff et al., 2017, 2020), an initial 40 km crust is evenly divided into upper (2800 kg/m^3) and lower (2900 kg/m^3) layers, following wet quartzite (Gleason and Tullis, 1995) and wet anorthite (Rybacki et al., 2006) dislocation creep flow laws, respectively. Although the crustal lithologic

structure is held constant, the bulk rheology of the crust (and mantle) varies as a function of the initial geothermal structure.

The mantle (3300 kg/m^3) viscous rheology is defined using flow laws for dry olivine (Hirth and Kohlstedt, 2003), with dislocation creep only in the mantle lithosphere and a composite of dislocation and diffusion creep in the asthenosphere (Table S1). Deformation during the initial stages of rifting is localized in the model center by delineating a 250 x 60 km zone of heterogeneous initial plastic strain (Fig. S1; after Pan et al., 2022).

Experimental Approach

We ran 16 rift-inversion models in 2D (Table 1). Each model began by developing either a narrow or wide rift from the initial block of continental lithosphere using variations in lithospheric strength and extension velocity. We adjusted lithospheric strength by changing the surface heat flow, which changes the geothermal gradient and thus the thickness of the mantle lithosphere, defined by a lithosphere-asthenosphere boundary (LAB) at the 1300°C isotherm. We created a narrow rift by slowly (0.5 cm/yr) extending a cold, thick lithosphere (120 km total, 80 km mantle lithosphere) and a wide rift by rapidly (2 cm/yr) extending a hot, thin lithosphere (80 km total, 40 km mantle lithosphere). This approach follows previous studies indicating that high extension velocity and weak lithosphere promote hyperextended, asymmetric rifting (e.g., Huismans and Beaumont, 2011; Brune et al., 2014; Tetreault and Buiter, 2018). We stop extension at the point of lithospheric breakup (i.e., first exposure of the asthenosphere) or halfway to the point of breakup in terms of time.

For each of these initial rift structures, we then vary the duration of post-rift cooling, during which horizontal velocities are set to 0. One set of models has no post-rift cooling phase (i.e., immediate inversion following extension), while a second set has a cooling period of 20 Myr. This cooling period was chosen to capture the initial effects of post-rift cooling, and we expect that additional cooling would further impact the structural style of rift-inversion orogens. For each of the resulting 8 combinations of rift structure and post-rift cooling, we impose 2 different convergence velocities during inversion (1 cm/yr, 5 cm/yr) that capture a range of typical convergent plate motion (e.g., Hatzfeld and Molnar, 2010), in order to compare the structures of rift-inversion orogens with convergence velocities comparable to those of plate-boundary orogens. We scaled the time of inversion (20 Myr, 4 Myr) so that each resulting orogen undergoes the same amount of total convergence (200 km). This allows direct comparison of orogenic style across models independent of the stage of orogenic evolution. Table S2 illustrates which variables (extension velocity, rift duration, post-rift cooling, convergence velocity) are changed when comparing each pair within the 16 models run.

Model Limitations

Our limited parameter sweep naturally excludes many possible rift geometries, post-rift cooling durations, and convergence velocities while seeking to establish first-order impacts these variables may have on the resulting orogens. In particular, we only examine rift inversion orogens resulting from rifts that have not been extended beyond the point of lithospheric breakup. We do not model this scenario specifically because our models do not account for

magmatism and the resulting production of oceanic lithosphere, which may significantly impact rheology and increase strain localization. The modeling of melting via two-phase flow is not yet feasible in ASPECT when using a viscoplastic rheology.

Summary of Model Tests

We conducted extensive tests of a reference rift inversion model to determine the optimal balance between model realism, stability, and computational efficiency in ASPECT. All model tests involved 12.5 Myr of extension at 1 cm/yr with a mantle lithosphere of 60 km thickness to bring a continental rift to breakup, followed by 20 Myr of inversion at 1 cm/yr (200 km shortening) to create a model orogen. The inversion phase in particular was prone to crashing with convergence errors in the linear solver of ASPECT as one side of the orogen was thrust beneath another, necessitating a careful choice of parameters that would allow underthrusting to take place successfully.

To increase model realism, we attempted to implement a viscoelastic-plastic rheological formulation, but this resulted in model instability when combined with particle-in-cell material tracking methods and composite creep in the asthenosphere. As a result, we adopted a viscoplastic rheology.

We tested increasing the range of permissible viscosities to between 1×10^{18} Pa s and 1×10^{26} Pa s but found that the large viscosity contrasts led to convergence errors and model instability when coupled with composite creep in the asthenosphere. Models ran most efficiently at a range of 1×10^{20} Pa s to 1×10^{26} Pa s, but we adopt the more realistic but still acceptably efficient range of 1×10^{19} Pa s to 1×10^{25} Pa s.

We attempted to increase the efficiency and accuracy of the particle-in-cell material tracking by using a bilinear least square interpolation scheme but found that, in the absence of a limiter, tracking of compositional fields on the model domain sides became highly inaccurate, with runaway increases in values that should not have exceeded 1. Instead, we use a cell averaging scheme for particle interpolation. We also fix vertical velocities and compositions on the sides of the models, in addition to having all inflow/outflow at the sides rather than the base, to ensure no errors occur in assignment of compositional fields to new material flowing into the model domain.

We initially used a model size of 1000 x 400 km with a global resolution of 1 km. This resolution was found to be excessively computationally expensive and resulted in very large file sizes for 2D models. We attempted to improve model efficiency and stability by employing adaptive mesh refinement (AMR), in which model resolution would be as low as 4 km in the asthenosphere and 1 km only in the crust and uppermost mantle. AMR improved model performance considerably and produced rifting models very similar to those at 1 km global resolution. However, there were significant differences in first-order structural style between inversion models with any component of AMR in a 1000 x 400 km model domain and inversion models with a global resolution of 1 km in a 1000 x 400 km model domain, due to variations in the convection cells that developed in the asthenosphere during inversion.

As a result, we expanded the size of our model domain to 1000 x 600 km to include more asthenosphere while continuing to allow improved efficiency via AMR. In our tests, AMR models with a 1000 x 600 km domain produced comparable results in both rifting and inversion models to our original 1000 km x 400 km global resolution models. To further confirm the validity of employing AMR in these models, we also re-ran Model 1 without AMR (Fig. S4; 1 km global resolution, 1000 x 600 km model domain), which produced nearly identical results to our Model 1 results with AMR reported in the main text and figures.

To test the effects of the geometry of the initial plastic strain zone, we re-ran Model 1 with an initial strain zone of 150 x 60 km instead of 250 x 60 km (Fig. S4). The result of this model was the same structural style as the original Model 1 (Style AU) but with opposing polarity of underthrusting. Changing the width of the strain zone also changes the semi-random distribution of strain, which likely led to localization along different structures, even though the overall style is the same.

We also re-ran Model 1 at slower convergence velocities (0.5 cm/yr and 0.2 cm/yr), with duration of inversion scaled (40 Myr, 100 Myr) to result in the same amount of total convergence (200 km). These models had less asymmetric underthrusting (Style AU) than Model 1 and instead exhibited more of the flip in thrust polarity reminiscent of Style PF, although the final orogens still exhibit distinctly asymmetric underthrusting.

We re-ran Model 2 with an additional 20 Myr of post-rift cooling (40 Myr of total post-rift cooling; Fig. S4) to test the effects of a more extended period of post-rift cooling, which may be expected for some rift-inversion orogens. This model overall displays a similar structural style to Model 2, with a combination of asymmetric underthrusting (AU) and polarity flip (PF), though in the model with extended cooling the sense of polarity (right-directed underthrusting) is opposite to that of Model 2 (left-directed underthrusting). This suggests that extended cooling likely will change the structure of rift-inversion orogens in detail, although the overall structural style may remain the same.

Comparisons with Prior Rift Inversion Models

Our study differs from prior work primarily in seeking to explore the range of structural variability in rift inversion orogenesis as a general process, rather than investigating a specific rift-inversion orogen or comparing rift-inversion models with compressional models that have no extension phase. Many prior modeling studies focus on recreating the present-day structure of the Pyrenees (Jammes et al., 2014; Dielforder et al., 2019; Jourdon et al., 2019). These studies thus explore a limited parameter space and report models either without altering initial rift state or convergence velocity (Dielforder et al., 2019) or with only minor variations in magnitude of extension and/or crustal rheology (Jammes et al., 2014; Jourdon et al., 2019). These models produced hyperextended rifts and rift-inversion orogens with significant asymmetric underthrusting comparable to the Pyrenees (Style AU), but the limited parameter space makes it difficult to identify the variables controlling the orogen asymmetry.

A few additional modeling studies have looked at rift-inversion orogenesis across a wider and more general parameter space. One compares model orogens formed from compression of a

uniform lithospheric block with those formed from inversion after 100 km of extension, with variations in crustal rheology and erosion (Jammes and Huismans, 2012). A second study similarly imposes 150 km of extension on a single model to compare resulting orogenic structure with models compressing a coherent lithospheric block (Wolf et al., 2021). The first-order structures of the resulting orogens in both studies are comparable to their compression-only counterparts, though the inversion models do create wider orogens with more mantle upwelling. A third study, strongly motivated by the structure of the High Atlas, inverts a symmetric rift after 70 km of extension, varying the post-rift cooling, the erosion rate during inversion, and the rheological properties of sediment deposited in the rift (Buiter et al., 2009). These models produce orogens exhibiting distributed lithospheric thickening (Style DT), with greater reactivation of the major rift-bounding normal faults being promoted by hotter thermal states, faster erosion, and weaker sediment. Although some restricted parameter space is explored in these examples, the range of variation is limited such that models do not vary significantly in terms of their first-order structural style.

Our models also differ from many prior rift-inversion models in terms of how brittle strain softening is modeled, with prior studies using initial to reduced internal friction angle ranges of 15°-2° (Jammes and Huismans, 2012; Jammes et al., 2014; Wolf et al., 2021), 30°-6° (Jourdon et al., 2019), and ~ 31.30°-2.87° (Dielforder et al., 2019). The weakened values in these ranges, particularly those of all studies other than Jourdon et al. (2019), represent the lower end of commonly assumed weakened values (see Naliboff et al., 2017 and 2020 for further discussion). The weakening parameterization is particularly significant for rift inversion problems, as absent strain healing, large portions of the lithosphere may have a significantly reduced brittle strength at the onset of compression. These lower weakened values in prior work may contribute to wider zones of deformation in the resulting orogen (>200 km wide) compared with our model results (~100 km wide) at similar magnitudes of convergence. We note that future work is needed to systematically test the effects of both amount and rate of strain weakening on the structural style of rift inversion orogens.

Model Parameter Files and Code

ASPECT parameter files for each of the 16 model runs and Python code used to prepare model runs, analyze results, and construct figures are available in a GitHub repository (https://github.com/dyvasey/riftinversion) and will be archived with a DOI using Zenodo upon manuscript acceptance.

References

Bahadori, A. et al., 2022, Coupled influence of tectonics, climate, and surface processes on landscape evolution in southwestern North America: Nature Communications, v. 13, p. 4437, doi:10.1038/s41467-022-31903-2.

Bangerth, W., Dannberg, J., Fraters, M., Gassmoeller, R., Glerum, A., Heister, T., and Naliboff, J., 2021, ASPECT v2.3.0:, https://doi.org/10.5281/ZENODO.5131909.

Brune, S., Heine, C., Pérez-Gussinyé, M., and Sobolev, S.V., 2014, Rift migration explains continental margin asymmetry and crustal hyper-extension: Nature Communications, v. 5, p. 4014, doi:10.1038/ncomms5014.

Brune, S., Kolawole, F., Olive, J.-A., Stamps, D.S., Buck, W.R., Buiter, S.J.H., Furman, T., and Shillington, D.J., 2023, Geodynamics of continental rift initiation and evolution: Nature Reviews Earth & Environment, v. 4, p. 235–253, doi:10.1038/s43017-023-00391-3.

Chapman, D.S., 1986, Thermal gradients in the continental crust: Geological Society, London, Special Publications, v. 24, p. 63–70, doi:10.1144/GSL.SP.1986.024.01.07.

Dielforder, A., Frasca, G., Brune, S., and Ford, M., 2019, Formation of the Iberian-European convergent plate boundary fault and its effect on intraplate deformation in Central Europe: Geochemistry, Geophysics, Geosystems, v. 20, p. 2395–2417, doi:10.1029/2018GC007840.

Duretz, T., de Borst, R., Yamato, P., and Le Pourhiet, L., 2020, Toward Robust and Predictive Geodynamic Modeling: The Way Forward in Frictional Plasticity: Geophysical Research Letters, v. 47, p. e2019GL086027, doi:10.1029/2019GL086027.

Fraters, M.R.T., Bangerth, W., Thieulot, C., Glerum, A.C., and Spakman, W., 2019, Efficient and practical Newton solvers for non-linear Stokes systems in geodynamic problems: Geophysical Journal International, v. 218, p. 873–894, doi:10.1093/gji/ggz183.

Fraters, M.R.T., and Billen, M.I., 2021, On the implementation and usability of crystal preferred orientation evolution in geodynamic modeling: Geochemistry, Geophysics, Geosystems, v. 22, p. e2021GC009846, doi:10.1029/2021GC009846.

Gassmöller, R., Lokavarapu, H., Heien, E., Puckett, E.G., and Bangerth, W., 2018, Flexible and Scalable Particle-in-Cell Methods With Adaptive Mesh Refinement for Geodynamic Computations: Geochemistry, Geophysics, Geosystems, v. 19, p. 3596–3604, doi:10.1029/2018GC007508.

Gleason, G.C., and Tullis, J., 1995, A flow law for dislocation creep of quartz aggregates determined with the molten salt cell: Tectonophysics, v. 247, p. 1–23, doi:10.1016/0040-1951(95)00011-B.

Glerum, A., Brune, S., Stamps, D.S., and Strecker, M.R., 2020, Victoria continental microplate dynamics controlled by the lithospheric strength distribution of the East African Rift: Nature Communications, v. 11, p. 2881, doi:10.1038/s41467-020-16176-x.

Glerum, A., Thieulot, C., Fraters, M., Blom, C., and Spakman, W., 2018, Nonlinear viscoplasticity in ASPECT: Benchmarking and applications to subduction: Solid Earth, v. 9, p. 267–294, doi:10.5194/se-9-267-2018.

Gouiza, M., and Naliboff, J., 2021, Rheological inheritance controls the formation of segmented rifted margins in cratonic lithosphere: Nature Communications, v. 12, p. 4653, doi:10.1038/s41467-021-24945-5.

Hatzfeld, D., and Molnar, P., 2010, Comparisons of the kinematics and deep structures of the Zagros and Himalaya and of the Iranian and Tibetan plateaus and geodynamic implications: Reviews of Geophysics, v. 48, p. RG2005, doi:10.1029/2009RG000304.

Heister, T., Dannberg, J., Gassmöller, R., and Bangerth, W., 2017, High accuracy mantle convection simulation through modern numerical methods – II: Realistic models and problems: Geophysical Journal International, v. 210, p. 833–851, doi:10.1093/gji/ggx195.

Heron, P.J., Peace, A.L., McCaffrey, K.J.W., Sharif, A., Yu, A.J., and Pysklywec, R.N., 2023, Stranding continental crustal fragments during continent breakup: Mantle suture reactivation in the Nain Province of Eastern Canada: Geology, v. 51, p. 362–365, doi:10.1130/G50734.1.

Hirth, G., and Kohlstedt, D., 2003, Rheology of the upper mantle and the mantle wedge: A view from the experimentalists: Geophysical Monograph-American Geophysical Union, v. 138, p. 83–106.

Huismans, R., and Beaumont, C., 2011, Depth-dependent extension, two-stage breakup and cratonic underplating at rifted margins: Nature, v. 473, p. 74–78, doi:10.1038/nature09988.

Jammes, S., and Huismans, R.S., 2012, Structural styles of mountain building: Controls of lithospheric rheologic stratification and extensional inheritance: Journal of Geophysical Research: Solid Earth, v. 117, doi:10.1029/2012JB009376.

Jammes, S., Huismans, R.S., and Muñoz, J.A., 2014, Lateral variation in structural style of mountain building: controls of rheological and rift inheritance: Terra Nova, v. 26, p. 201–207, doi:10.1111/ter.12087.

Jourdon, A., Le Pourhiet, L., Mouthereau, F., and Masini, E., 2019, Role of rift maturity on the architecture and shortening distribution in mountain belts: Earth and Planetary Science Letters, v. 512, p. 89–99, doi:10.1016/j.epsl.2019.01.057.

Kronbichler, M., Heister, T., and Bangerth, W., 2012, High accuracy mantle convection simulation through modern numerical methods: Geophysical Journal International, v. 191, p. 12–29, doi:10.1111/j.1365-246X.2012.05609.x.

Magni, V., Naliboff, J., Prada, M., and Gaina, C., 2021, Ridge jumps and mantle exhumation in back-arc basins: Geosciences, v. 11, p. 475, doi:10.3390/geosciences11110475.

Naliboff, J.B., and Buiter, S.J.H., 2015, Rift reactivation and migration during multiphase extension: Earth and Planetary Science Letters, v. 421, p. 58–67, doi:10.1016/j.epsl.2015.03.050.

Naliboff, J.B., Buiter, S.J.H., Péron-Pinvidic, G., Osmundsen, P.T., and Tetreault, J., 2017, Complex fault interaction controls continental rifting: Nature Communications, v. 8, p. 1179, doi:10.1038/s41467-017-00904-x.

Naliboff, J.B., Glerum, A., Brune, S., Péron-Pinvidic, G., and Wrona, T., 2020, Development of 3-D rift heterogeneity through fault network evolution: Geophysical Research Letters, v. 47, p. e2019GL086611, doi:https://doi.org/10.1029/2019GL086611.

Pan, S., Naliboff, J., Bell, R., and Jackson, C., 2022, Bridging Spatiotemporal Scales of Normal Fault Growth During Continental Extension Using High-Resolution 3D Numerical Models: Geochemistry, Geophysics, Geosystems, v. 23, p. e2021GC010316, doi:10.1029/2021GC010316.

Rose, I., Buffett, B., and Heister, T., 2017, Stability and accuracy of free surface time integration in viscous flows: Physics of the Earth and Planetary Interiors, v. 262, p. 90–100, doi:10.1016/j.pepi.2016.11.007.

Rybacki, E., Gottschalk, M., Wirth, R., and Dresen, G., 2006, Influence of water fugacity and activation volume on the flow properties of fine-grained anorthite aggregates: Journal of Geophysical Research: Solid Earth, v. 111, doi:https://doi.org/10.1029/2005JB003663.

Sandiford, D., Brune, S., Glerum, A., Naliboff, J., and Whittaker, J.M., 2021, Kinematics of Footwall Exhumation at Oceanic Detachment faults: Solid-Block Rotation and Apparent Unbending: Geochemistry, Geophysics, Geosystems, v. 22, p. e2021GC009681, doi:10.1029/2021GC009681.

Tetreault, J.L., and Buiter, S.J.H., 2018, The influence of extension rate and crustal rheology on the evolution of passive margins from rifting to break-up: Tectonophysics, v. 746, p. 155–172, doi:10.1016/j.tecto.2017.08.029.

Weerdesteijn, M.F.M., Naliboff, J.B., Conrad, C.P., Reusen, J.M., Steffen, R., Heister, T., and Zhang, J., 2023, Modeling Viscoelastic Solid Earth Deformation Due To Ice Age and Contemporary Glacial Mass Changes in ASPECT: Geochemistry, Geophysics, Geosystems, v. 24, p. e2022GC010813, doi:10.1029/2022GC010813.

Wolf, S.G., Huismans, R.S., Muñoz, J.-A., Curry, M.E., and Beek, P. van der, 2021, Growth of Collisional Orogens From Small and Cold to Large and Hot—Inferences From Geodynamic Models: Journal of Geophysical Research: Solid Earth, v. 126, p. e2020JB021168, doi:https://doi.org/10.1029/2020JB021168.

Table S1: Material Properties for Compositional Layers

	Upper Crust	Lower Crust	Mantle Lithosphere	Asthenosphere[1]	
Reference Density ($kg\ m^{-3}$)	2800	2900	3300	3300	
Flow Law[2]	Wet quartzite	Wet anorthite	Dry olivine	Dry olivine (dislocation)	Dry olivine (diffusion)
Viscosity Prefactor (A) ($Pa^{-n}\ m^{-p}\ s^{-1}$)	8.57×10^{-28}	7.13×10^{-18}	6.52×10^{-16}	6.52×10^{-16}	2.37×10^{-15}
Stress exponent (n)	4	3	3.5	3.5	-
Grain size (d) (m)	-	-	-	-	1×10^{-3}
Grain size exponent (m)	-	-	-	-	3
Activation energy (Q) ($kJ\ mol^{-1}$)	223	345	530	530	375
Activation volume (V) ($m^3\ mol^{-1}$)	-	-	-	-	18×10^{-6}
Specific heat (Cp) ($J\ kg^{-1}\ K^{-1}$)	750	750	750	750	
Thermal conductivity (k) ($W\ m^{-1}\ K^{-1}$)	2.5	2.5	2.5	2.5	
Thermal expansivity (α) (K^{-1})	2×10^{-5}	2×10^{-5}	2×10^{-5}	2×10^{-5}	
Heat production (H) ($W\ m^{-3}$)	1×10^{-6}	0.25×10^{-6}	0	0	
Friction angle[3] (°)	30	30	30	30	
Cohesion[3] (MPa)	20	20	20	20	

1. Asthenosphere viscous rheology determined by harmonic averaging of dislocation and diffusion creep flow laws.
2. Source for flow laws: wet quartzite (Gleason and Tullis, 1995), wet anorthite (Rybacki et al., 2006), dry olivine (Hirth and Kohlstedt, 2003).
3. Friction angle and cohesion decrease linearly by a factor of 0.375 between plastic strain values of 0.5 and 1.5 to simulate strain weakening.

Table S2: Model Pairs in which 1 Variable Is Changed

Model comparisons showing impact of rift mechanics (0.5 vs. 2 cm/yr Extension Velocity)

Model Pair	Extension Velocity (varied)	Rift Duration	Post-Rift Cooling	Inversion Velocity
1,5	0.5 or 2 cm/yr	Halfway (16 Myr)	0 Myr	1 cm/yr
2,6	0.5 or 2 cm/yr	Halfway (16 Myr)	20 Myr	1 cm/yr
3,7	0.5 or 2 cm/yr	Full Breakup (32 Myr)	0 Myr	1 cm/yr
4,8	0.5 or 2 cm/yr	Full Breakup (32 Myr)	20 Myr	1 cm/yr
9,13	0.5 or 2 cm/yr	Halfway (16 Myr)	0 Myr	5 cm/yr
10,14	0.5 or 2 cm/yr	Halfway (16 Myr)	20 Myr	5 cm/yr
11,15	0.5 or 2 cm/yr	Full Breakup (14.5 Myr)	0 Myr	5 cm/yr
12,16	0.5 or 2 cm/yr	Full Breakup (14.5 Myr)	20 Myr	5 cm/yr

Model comparisons showing impact of rift duration (halfway vs. full breakup)

Model Pair	Extension Velocity	Rift Duration (varied)	Post-Rift Cooling	Inversion Velocity
1,3	0.5 cm/yr	Halfway or Full Breakup	0 Myr	1 cm/yr
2,4	0.5 cm/yr	Halfway or Full Breakup	20 Myr	1 cm/yr
5,7	2 cm/yr	Halfway or Full Breakup	0 Myr	1 cm/yr
6,8	2 cm/yr	Halfway or Full Breakup	20 Myr	1 cm/yr
9,11	0.5 cm/yr	Halfway or Full Breakup	0 Myr	5 cm/yr
10,12	0.5 cm/yr	Halfway or Full Breakup	20 Myr	5 cm/yr
13,15	2 cm/yr	Halfway or Full Breakup	0 Myr	5 cm/yr
14,16	2 cm/yr	Halfway or Full Breakup	20 Myr	5 cm/yr

Model comparisons showing impact of post-rift cooling (0 vs. 20 Myr)

Model Pair	Extension Velocity	Rift Duration	Post-Rift Cooling (varied)	Inversion Velocity
1,2	0.5 cm/yr	Halfway (16 Myr)	0 or 20 Myr	1 cm/yr
3,4	0.5 cm/yr	Full Breakup (32 Myr)	0 or 20 Myr	1 cm/yr
5,6	2 cm/yr	Halfway (7.3 Myr)	0 or 20 Myr	1 cm/yr
7,8	2 cm/yr	Full Breakup (14.5 Myr)	0 or 20 Myr	1 cm/yr
9,10	0.5 cm/yr	Halfway (16 Myr)	0 or 20 Myr	5 cm/yr
11,12	0.5 cm/yr	Full Breakup (32 Myr)	0 or 20 Myr	5 cm/yr
13,14	2 cm/yr	Halfway (7.3 Myr)	0 or 20 Myr	5 cm/yr
15,16	2 cm/yr	Full Breakup (14.5 Myr)	0 or 20 Myr	5 cm/yr

Model comparisons showing impact of convergence velocity (1 vs. 5 cm/yr)

Model Pair	Extension Velocity	Rift Duration	Post-Rift Cooling	Inversion Velocity (varied)
1,9	0.5 cm/yr	Halfway (16 Myr)	0 Myr	1 or 5 cm/yr
2,10	0.5 cm/yr	Halfway (16 Myr)	20 Myr	1 or 5 cm/yr
3,11	0.5 cm/yr	Full Breakup (32 Myr)	0 Myr	1 or 5 cm/yr
4,12	0.5 cm/yr	Full Breakup (32 Myr)	20 Myr	1 or 5 cm/yr
5,13	2 cm/yr	Halfway (7.3 Myr)	0 Myr	1 or 5 cm/yr
6,14	2 cm/yr	Halfway (7.3 Myr)	20 Myr	1 or 5 cm/yr
7,15	2 cm/yr	Full Breakup (14.5 Myr)	0 Myr	1 or 5 cm/yr
8,16	2 cm/yr	Full Breakup (14.5 Myr)	20 Myr	1 or 5 cm/yr

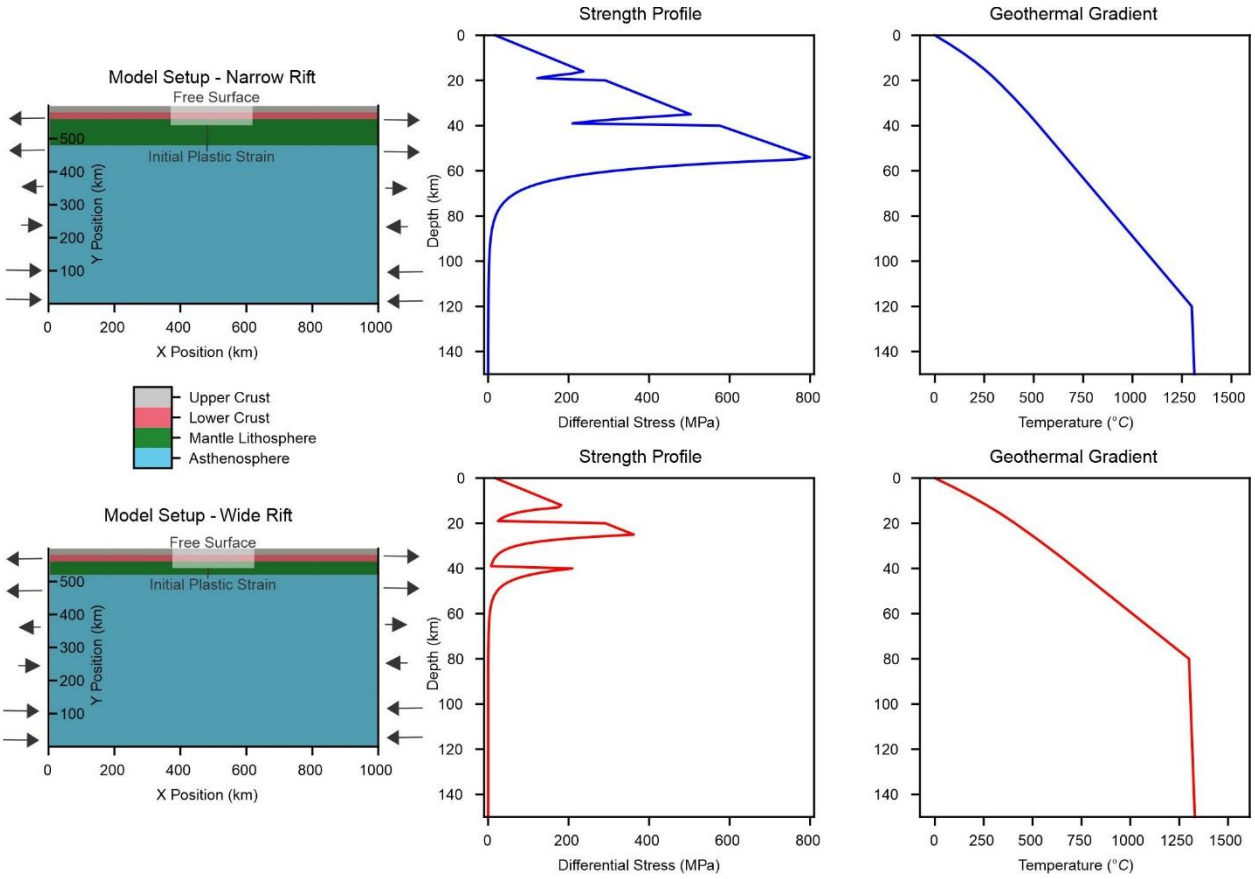

Figure S1: Initial conditions for rift inversion models with a narrow rift (top row) and a wide rift (bottom row). Models consist of a 1000x600 km box divided into compositional fields for upper crust, lower crust, mantle lithosphere, and asthenosphere, with total lithosphere thickness of 120 km in narrow rift models and 80 km in wide rift models. Arrows on either side of the setup diagrams show material flow directions during the rifting phase, with outflow on the model sides in the top half of the model is balanced from inflow on the model sides in the bottom half of the model. A 250x60 km zone of randomized initial plastic strain (gray box) helps localize strain in the center of the model. Effective strength, shown for a reference strain rate of 1 x 10^{-15} s^{-1}, is a combination of dislocation/diffusion creep viscous rheology and Drucker-Prager plasticity (Table S1); the geothermal gradient is modified by changing surface heat flow so that the base of the lithosphere is at 1300°C.

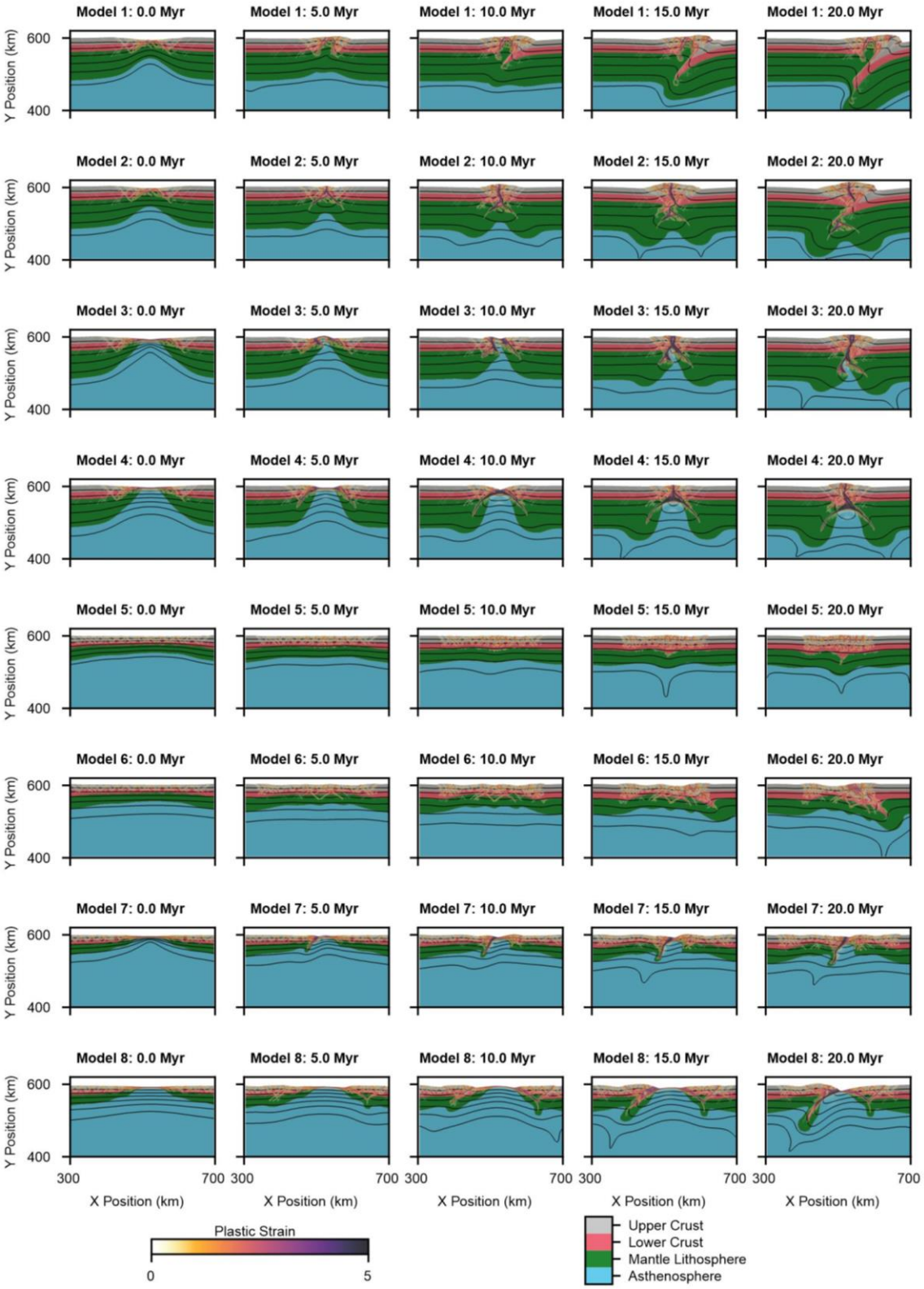

Figure S2: Model orogen results during the inversion phase for all models with a convergence velocity of 1 cm/yr.

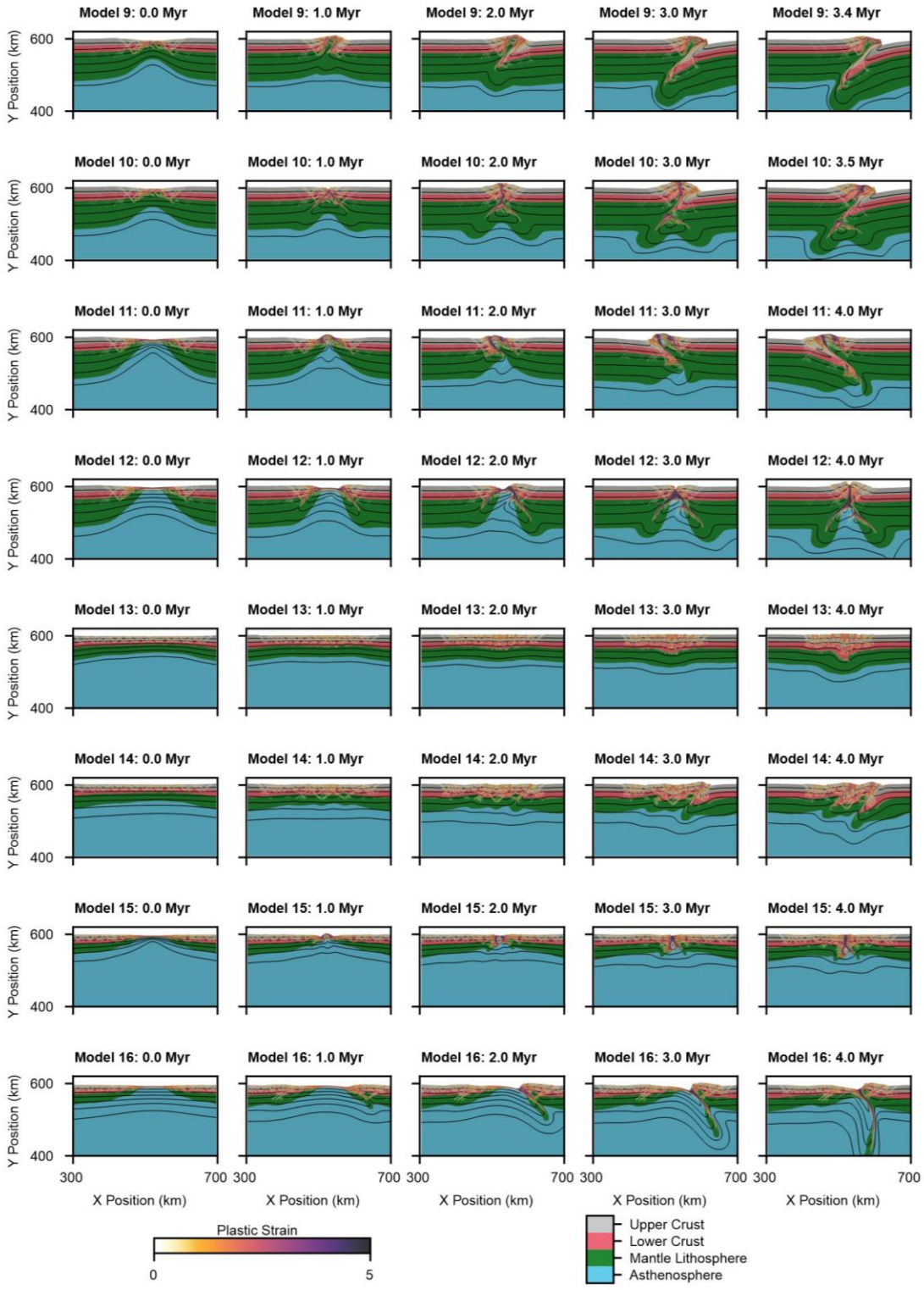

Figure S3: Model orogen results during the inversion phase for all models with a convergence velocity of 5 cm/yr.

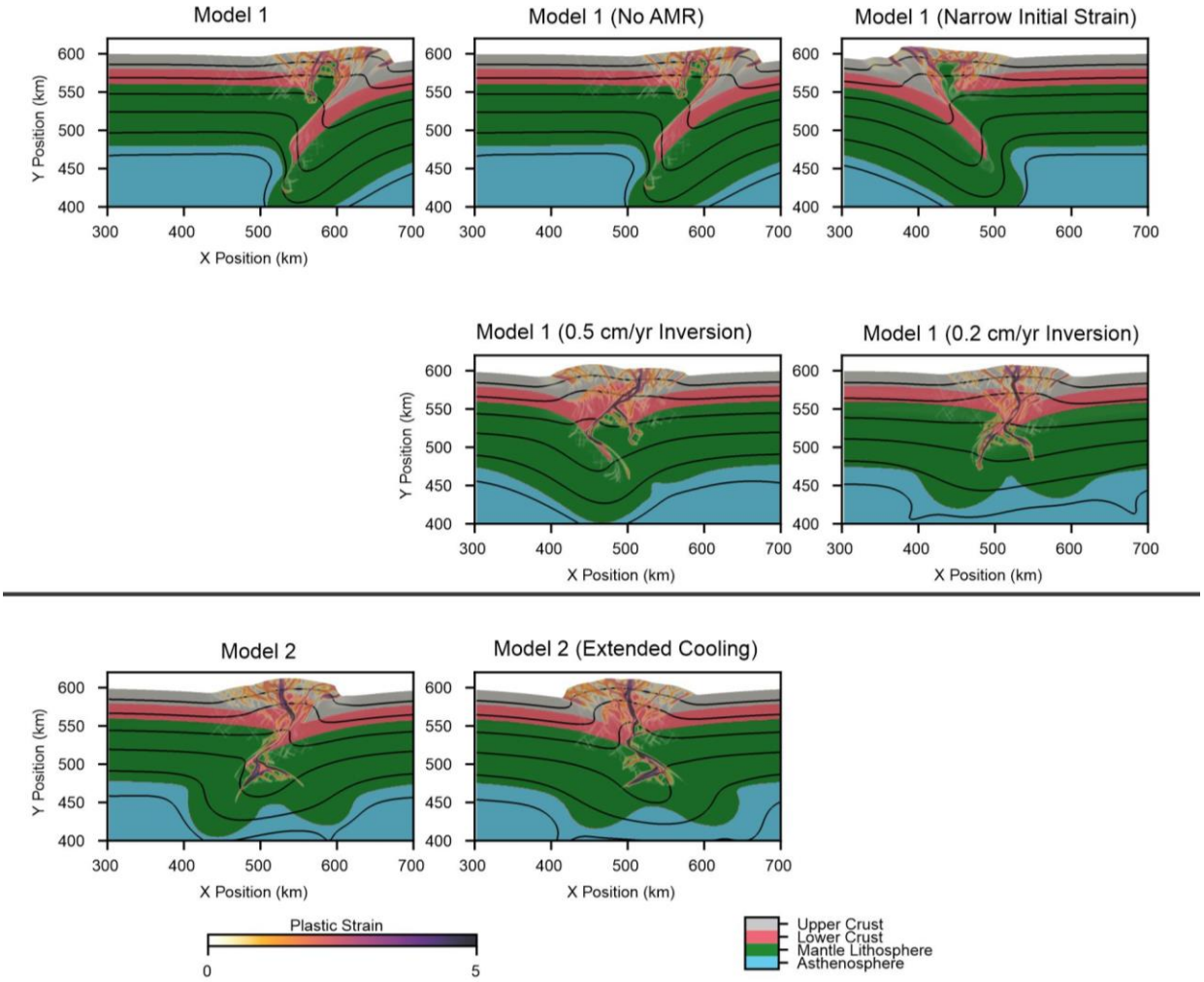

Figure S4: Summary of additional models run to test the effects of resolution, size of the initial plastic strain zone, slower convergence velocity, and extended post-rift cooling, as discussed in the supplementary text. Four modified versions of Model 1 were run: one with 1 km global resolution instead of adaptive mesh refinement (No AMR), one with a 150 x 60 km initial plastic strain zone instead of 250 x 60 km (Narrow Initial Strain), one with 0.5 cm/yr convergence velocity (200 km total convergence) instead of 1 cm/yr, and one with 0.2 cm/yr convergence velocity (200 km total convergence). A modified version of Model 2 was run with 40 Myr of post-rift cooling (Extended Cooling) instead of 20 Myr.